A Steady State Semi-analytical Approximation of Melt Pool Evolution in Pulsed Laser Surface Melting

Utsavkumar Mistry[a], Madhu Vadali[b*]

[a]*SMART Lab, Mechanical Engineering Discipline, IIT Gandhinagar, Gujarat, India*

[b]*SMART Lab, Jointly with Mechanical Engineering & Electrical Engineering Disciplines, IIT Gandhinagar, Gujarat, India*

**Corresponding author, email: madhu.vadali@iitgn.ac.in*

Abstract

Pulsed laser surface melting (pLSM) is a technique that offers efficient and effective way to modify the geometry surfaces without any addition or removal of material. The resultant surface geometry plays a critical role in several applications. This paper presents a steady state thin film approximation of the meltpool created by pLSM and the resulting semi-analytical solution for the evolved surface geometry. This predictions of the semi-analytical solution are then compare with a validated numerical solution. The comparison demonstrate a good match with errors ranging from ~4% to ~25% across several pulse duration. Larger errors are observed at comparatively lower and higher pulse duration, and smaller errors are observed for intermediate pulse duration values. Overall, the thin film solution is a reasonable and useful approximation of the of the evolved surface geometry through pLSM process, thus saving significant computational costs.

Keywords: Laser surface melting, surface tension, thin film approximation, surface geometry

NOTATIONS AND NOMENCLATURE

$[*]^*$	Dimensional quantity	P	Laser peak power, W
$[*]^T$	Transpose operator	R_b	Laser beam radius, μm
$[*]^{(0)}$	Order 1 parameter	τ_t^*, τ_n^*	Tangential and Normal stress tensor at free surface
$\underline{\nabla}^*$	Gradient operator	$\underline{\underline{\tau}}^*$	Viscous stress tensor
ρ	Density, kg/m^3	$(\partial\gamma^*/\partial T^*)$	Surface tension coefficient, $N/m-K$
c_p'	Equivalent specific heat, $J/kg-K$	L	Latent heat of fusion, J/K
T^*	Temperature, K	T_s	Solidus temperature, K
t^*	Time, s	T_m	Melting temperature, K
$\underline{V}^*$	Velocity vector, m/s	T_l	Liquidus temperature, K
k	Thermal conductivity, $W/m-K$	T_v	Evaporation temperature, K
p^*, p_c	Pressure and its characteristic value, Pa	T_i	Initial temperature, K
μ	Dynamic viscosity, $kg/m-s$		

ν	Kinematic viscosity, m^2/s
t_p	Pulse duration, μs
r^*	Radial position, μm
R	Computational domain radius, μm
z^*	Vertical position, μm
Z	Computational domain height, μm
h^*	Free surface height function, μm
u_r^*, U_R	Velocity and its characteristic value in r direction, m/s
u_z^*, U_z	Velocity and its characteristic value in z direction, m/s
l_c	Characteristic value in r-direction, μm
z_c	Characteristic value in z-direction, μm
$\hat{t}, \hat{n}$	Unit tangent and normal vector at free surface
α	Absorptivity
q^*	Heat flux, $W/\mu m^2$
γ^*, γ_0	Surface tension and its characteristic value, N/m

Non-dimensional quantities

r	Radial coordinate
z	Vertical coordinate
u_r	Velocity component in r-direction
u_z	Velocity component in z-direction
h	Free surface height function
p	Pressure
t	Time
θ	Temperature
q	Heat flux
Re	Reynolds number
Pe	Peclet number
Ca	Capillary number

1 Introduction

Laser surface melting is a non-traditional, effective and efficient manufacturing process that has been increasingly used for generating micro-scale surface features on metallic components without addition or removal of material [1]. Creating a near flat feature to reduce surface roughness, also known as polishing, is an application of laser surface melting that has been widely studied recently. Several experimental studies have successfully demonstrated that polishing via laser surface melting is an effective alternative to other polishing techniques such as coatings, chemical polishing, abrasive polishing, etc. [1, 2].

In laser surface melting (LSM), a continuous wave or pulsed laser source irradiates a surface. This heats the material and eventually melts a thin layer on the surface, creating a melt pool. Complex flows within the melt pool, primarily under viscous and surface tension forces, result in the dynamic evolution of the surface and upon resolidification results in new surface features. While conductive heat transfer is dominant in the initial stages of surface melting, convection heat transfer dominates the later stages in molten state. Among continuous wave and pulsed sources, pulsed laser sources have the advantage of smaller melt pool sizes while producing the desired final surface. Thus, there is minimal modification of material morphology and the bulk properties of the workpiece material are conserved.

In pulsed laser surface melting (pLSM), the evolution of the surface and the geometry of the surface feature depends on process properties such as incident laser power, pulse duration and incident beam diameter. There are few studies that try to capture the effects of various process parameters in pulsed laser surface melting in the context of determining final surface evolution. While most of the works are experimental [3–6], some have developed complex

multi-physics numerical models to investigate the evolution of the final surface after melting [7–9]. Numerical studies done in [10] demonstrate that buoyancy forces in the melt pool during laser surface melting can be neglected. They have considered non-deformable free flat surface to find the velocity and temperature distribution in melt pool of rectangular cavity shape. In this context, studies done at the University of Wisconsin Madison [3,11] are of particular interest as they have systematically demonstrated the effects of temperature gradients of surface tension on surface evolution due to laser micro melting. Ma el al. [11] have developed a numerical model and showed that the resultant surface geometry matches well with experimental values. Their work will be used to validate the work done in this paper.

For axisymmetric flow under gaussian beam distribution, analytical solutions of the heat conduction equation is obtained by Woodard et al. [12] and provide initial estimates of temperature distribution and hardened spot size. Tokarev et al. [13] presented an analytical estimation for melt depth using a one dimensional transient heat conduction in pulsed laser melting. They have given overestimate and underestimate values for melt depth which depends on various property values of material and laser pulse duration (t_p). They have shown a good match with experiments. Their results will be used in the current current work. A limitation among all these studies is that the analysis was done under non-deformable free surface of the material and haven't considered stress balance conditions at free surface. Subsequently, two dimensional numerical simulations were performed [14] to showcase the deformation of free surface under steady state and transient condition. Analytical similarity solution for velocity profile and temperature distribution was given by [15] for marangoni convected flow over flat surface. They have assumed the formation of boundary layer on flat free surface under imposed temperature gradient. While these are useful in deriving insights into the process, no studies exist that can provide for a analytical or semi-analytical solution for the evolution of the surface geometry, which ulmitately play a key role in several applications ranging from bio-implants to micro-fluiding channels. The present study, therefore focusses to develop a semin-analytical solution for prediction of surface geometry.

In this work, a two dimensional transient axisymmetric numerical model with a deformable free surface will be developed for pulsed laser surface melting. This model will include temperature dependent material properties and will act as a baseline model the semi-analytical solution. For rigor, it will be shown that this model compares well with the results presented in Ma et al. [11]. Next, a steady state semi-analytical experession will be derived for the surface geometry using a thin film approximation. It will be shown that the predictions of the this semi-analytical solution match closely with the numerical results with certain caviats. Finally, a detailed discussion on the results will be provided highlight the advantages and more importantly, the limitations of the semi-analytical solution.

2 Physics of Pulsed Laser Surface Melting

2.1 Mechanism of pulsed laser surface melting

pLSM is a multi-physics process consisting heating of a micro scaled metal surface asperities beyond the melting and below the ablation temperature, using laser pulses. This complex process involves heat transfer primarily through conduction and convection, phase change of material

and resulting flow of the melt. Once material is in molten state, it starts to redistribute under influence of surface tension, pressure and viscous forces until material is resolidified. The mechanism of pLSM can be easily understood with the following four stages:

Stage 1: Heating

In this stage, the surface of the material is heated by the incident laser beam and the heat is conducted into the metal. As shown in Figure 1(a), conduction continues and the temperature at center point (shown in blue) of metal reaches the melting temperature. At this temperature, the material begins to melt by absorbing energy equivalent to its latent heat of fusion before changing phase. Note that in case of alloys, there is no single temperature at which the material melts, but the melting happens from solidus temperature, the temperature in metal below which the entire metal is in solid phase, to the liquidus temperature, above which the entire metal is in liquid phase.

Stage 2: Melting

This stage begins when the surface temperature is beyond the liquidus temperature (melting temperature for pure metals). The heat is transferred into the material through conduction and convection modes. The metal continues to melt and melt pool size increases in both radial and axial directions. Figure 1(b) shows the ascending melt-front, as the liquidus temperature isothermal contour, as it moves into the bulk of the material. This melt pool size continues to increase until the laser pulse is ON. The direction of the molten metal flow depends on the value of surface tension coefficient ($\partial\gamma^*/\partial T^*$) which will be discussed in Section 2.2.

Stage 3: Solidification

Solidification begins once the incident heat source is switched off. In this stage the conduction and convection of heat in the melt pool continue to slightly increase the melt pool size before solidification begins. At this point, the melt pool continues to lose energy as conduction into the bulk and a small amount as radiation to the environment. Figure 1(c) shows the solidification-front, as the liquidus temperature isothermal contour, receding from the bulk of the material toward the surface.

Stage 4: Cooling

In this stage, the entire molten material has resolidified. The solid material continues to cool down by conducting heat into the bulk and losing little heat as radiation. The stage is complete once the material returns back to its original temperature, usually at room temperature.

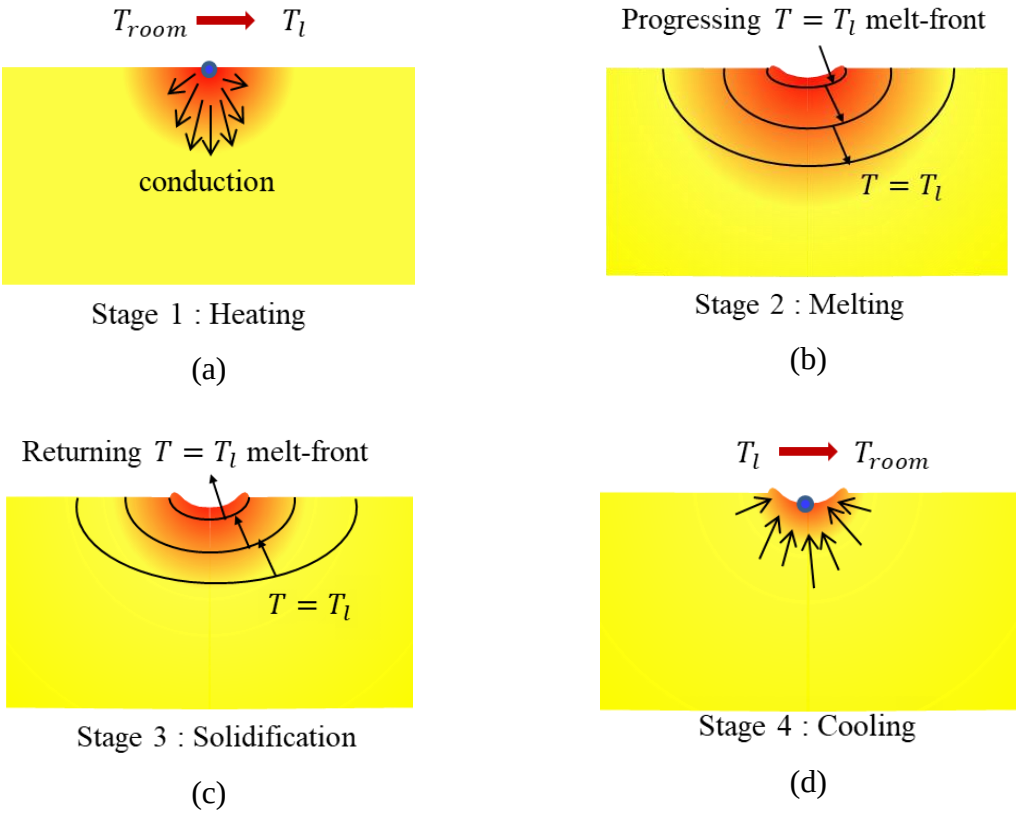

Figure 1: Four stages of pLSM process

2.2 Effect of surface tension gradient

In Stages 2 & 3 of pLSM, the metal is in a molten state of a metal. A large gradient of temperature exists across the melt pool surface. This creates a gradient in the surface tension and thus causing an force imbalance across the surface. This imbalance in surface tension coupled with viscous forces causes the molten metal to flow. This phenomenon is called the Marangoni effect and the resulting flows are called thermocapillary flows. The nature of the flows and the behavipor of the molten material are dictated by the surface tension coefficient, $\partial\sigma^*/\partial T^*$, of the material.

Typical power distribution of a laser beam is Gaussian, i.e., the intensity at the center of the beam is maximum and it exponential decays to zero towards the edges. Therefore, the temperature at center of the melt pool is much higher than that at the edge. Materials with a negative surface tension coefficient will have higher surface tension at the edges than the center of the meltpool. This creates gradients of surface tension and flow of molten metal takes place from low surface tension to higher surface tension. This process develops the upwelling of material from center point towards the edge of molten pool as shown in Figure 2. Conversely, a positive surface tension coefficient results in upwelling of the material towards the center of the pool.

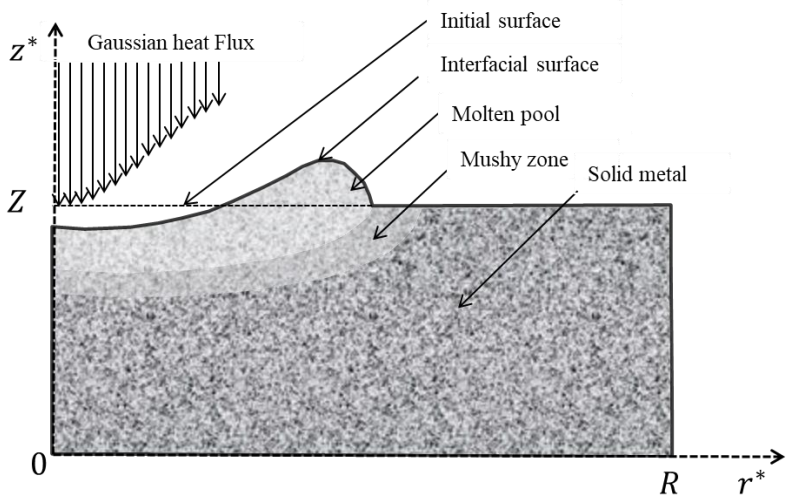

Figure 2: Schematic of solidified surface geometry for materials with negative $\boldsymbol{\partial\sigma^*/\partial T^*}$

3 Numerical model of pLSM

To capture the physics of the process, a numerical model is developed and is simulated using COMSOL commercial software for simulation purpose. Axisymmetric model is the natural choice of for numerical analysis, as within each cycle of melting and solidification, the process is inherently symmetric about the central axis of the incident laser beam. Further, sufficient time is provided between two laser pulses to ensure the material returns to its room temperature. Therefore, studying the process under a single pulse is sufficient. is sufficient to study the process. This numerical model will also act as a reference to validate the semi-analytical results to be discussed later in the paper. In this section, this model is detailed with the validation results.

3.1 Governing equations and assumptions

For modelling simplicity and ease, the following assumptions are made:

- The material is isotropic and homogeneous.
- Chemical changes are ignored as the process is typically carried out in an inert environment.
- Radiation and convection heat losses to the surroundings are neglected.
- Newtonian flow is assumed in melt pool, i.e., constant viscosity.
- The surface tension of the molten material is varying linearly with temperature.
- The gravitational forces [3] and buoyancy forces [16] are neglected as they are considerably small as compared to the surface tension effects.
- Ablation is not modeled as maximum temperature is ensued to be not beyond vaporization temperature of material.
- There is no additional source irradiating on surface.

Under the above assumptions, the coupled temperature and velocity fields are given by the energy conservation equation and the Navier-Stokes equation and are given by the following,

$$\rho c_p' \left(\frac{\partial T^*}{\partial t^*} + \underline{V}^* \cdot \underline{\nabla}^* T^*\right) - \underline{\nabla}^* \cdot \left(k \underline{\nabla}^* T^*\right) = 0 \tag{1}$$

$$\rho \left[\frac{\partial \underline{V}^*}{\partial t^*} + \left(\underline{V}^* \cdot \underline{\nabla}^*\right) \underline{V}^* \right] = -\underline{\nabla}^* p^* + \underline{\nabla}^* \cdot \left\{ \mu \left[\left(\underline{\nabla}^* \underline{V}^*\right) + \left(\underline{\nabla}^* \underline{V}^*\right)^T \right] \right\} \tag{2}$$

where, c_p' is equivalent specific heat which accounts latent heat of fusion, k is thermal conductivity, μ is dynamic viscosity of a material. Further, under the assumption of steady flow of the molten material, the continuity equation is written as,

$$\underline{\nabla}^* \cdot \underline{V}^* = 0 \tag{3}$$

3.2 Interfacial and boundary conditions

Normal and tangential stress is developed on the interface between affected surface area and surrounding environment. Stress balance in normal and tangential direction on interface is as follows,

Normal Stress Balance $$-p^* + \left(\underline{\underline{\tau}}^* \cdot \hat{n}\right) \cdot \hat{n} = \gamma^* \left(\underline{\nabla}^* \cdot \hat{n}\right) \tag{4}$$

Tangential Stress Balance $$\left(\underline{\underline{\tau}}^* \cdot \hat{n}\right) \cdot \hat{t} = \left(\partial \gamma^* / \partial T^*\right)\left(\underline{\nabla}^* T^* \cdot \hat{t}\right) \tag{5}$$

where γ^* is the surface tension and $\underline{\nabla}^* \cdot \hat{n}$ is the curvature of the surface. The laser beam source incident on the surface is modelled as a heat flux boundary condition on initially flat surface is given by,

$$\hat{n} \cdot \left(k \underline{\nabla}^* T^*\right) = \alpha q^* \tag{6}$$

where q^* is heat flux and α is the absorptivity. Gaussian distribution of heat flux within pulse duration is assumed and is given by,

$$q^* = \frac{P}{\pi R_b^2} e^{\left(-\frac{2r^{*2}}{R_b^2}\right)} \tag{7}$$

where P is the peak power of gaussian distribution and R_b is the laser beam radius.

Boundaries $r^* = R$ and $z^* = 0$ in Figure 2 are considered stationary as material has no velocity at these boundaries. Therefore, no slip conditions are appropriate to imposed at these boundaries. Further, adiabatic boundary conditions are assumed at $r^* = R$ and $z^* = 0$ as these are sufficiently far from the melt pool to ensure no heat or mass transfer with the surroundings. These are mathematically described as,

$$\underline{V}^*(0, r^*) = 0 \;\&\; \underline{V}^*(z^*, R) = 0 \tag{8}$$

$$\hat{n} \cdot \left(k \underline{\nabla}^* T^*\right)\big|_{(0, r^*)} = 0 \;\&\; \hat{n} \cdot \left(k \underline{\nabla}^* T^*\right)\big|_{(z^*, R)} = 0 \tag{9}$$

3.3 Material properties

Without loss of generality, Ti6Al4V alloy is the material of choice for all the work presented in this paper. Temperature dependent properties of Ti6Al4V, viz., density, thermal

conductivity, specific heat and dynamic viscosity, are taken for the numerical simulations [17,18]. Effective viscosity method is used to enable the solid material to stationary position and molten metal to flow [16]. For convergence, the solid state viscosity is set to be approximately 30 million times of liquid state viscosity. The value of surface tension coefficient is used for pure titanium in air ($\partial\sigma^*/\partial T^*$ = -0.26 $mN/m-K$ [19]), as it was not found in literature for Ti6Al4V alloy. As $\partial\sigma^*/\partial T^*$ plays an important role, this value would build some error in simulating final surface geometry. Absorptivity value is taken as 0.5 [12]. Table 1 shows some properties used in simulation.

Table 1: Parameters and constants used in simulations

Computational dimensions (R x Z) (μm)	120 x 30
Solidus temperature, T_s (K) [20]	1877
Melting temperature, T_m (K) [20]	1903
Liquidus temperature, T_l (K) [17]	1923
Evaporation temperature, T_v (K) [18]	3500
Ambient temperature, T_{amb} (K)	298
Initial temperature, T_i (K)	298
Latent heat of fusion, L (J/K) [17]	3.24×10^5

3.4 Meshing and solver

Computational domain was meshed with free triangular and finer mesh element. As material will flow once the metal is in molten state, moving mesh was applied to meshed geometry and mesh element size was calibrated for fluid dynamics. Direct solver PARDISO used in simulation requires less RAM then other solvers and can store the solution out-of-core [21]. Laplace mesh smoothing method ensures smooth deformations of mesh, given the constraints on boundaries of domain.

3.5 Model validation

The model was validated by comparing the melt pool geometry and normalized peak to valley height (PVH) to those discussed in Ma et al. [11]. Although the application in [11] laser micro polishing of metallic surfaces, as discussed earlier, it is a specific application of pLSM. Note that the model by Ma et al. was validated against experimental laser polishing results on Ti6Al4V and therefore, this model-to-model validation is acceptable. The results of both the models are within $\pm$7% of error. These are summarized in following Table 2.

Table 2: Validation of numerical simulation model

t_p (μs)	Normalized PVH (μm)		%Error
	Ma et al [11]	Current work	
1	0.01	0.0105	-5
3	0.06	0.056	6.66
5	0.12	0.113	5.83

4 Non-dimensionalization of equations

The mathematical model of the process described in Sections 3.1 and 3.2 are non-dimesionalized for ease of analysis. Further, Non-dimensionalization results in dimensionless numbers through which material independent insights into the process can be easily derived without the need to run complex numerical simulations. This section details the procedure of non-dimensionalization under the following assumptions:

- Only steady state equations are considered i.e., the temporal variations of temperature, pressure, velocity are neglected. Although this is only true when the meltpool is in molten state for sufficiently long durations, it will be shown later in the the paper that this analysis will result in useful estimates of the surface geometry.
- Temperature dependence of material properties is neglected and constant properties at liquidus temperature are used. These are tabulated in Table 3.

Under the above assumptions, Equations (1) - (6) are non-dimensionalised and are summarized in Table 4. A detailed derivation of the these equations is given in Appendix A.

Table 3: Constant properties at liquidus temperature

Thermal conductivity, k $(W/m-K)$	30
Surface tension coefficient, $(\partial\gamma^*/\partial T^*)$ $(\mathrm{m}N/m-K)$	-0.26
Surface tension, γ_0 (N/m)	1.65
Density, ρ (kg/m^3)	3886
Specific heat, c_p $(J/kg-K)$	800
Dynamic viscosity, μ $(kg/m-s)$	0.005

Table 4: Steady State Dimensionless Equations for pLSM

Navier-Stokes Equations

R-momentum
$$\epsilon^2 Re\left[\left(u_r\frac{\partial u_r}{\partial r}\right)+\left(u_z\frac{\partial u_r}{\partial z}\right)\right]=-\frac{\partial p}{\partial r}+\epsilon^2\frac{\partial}{\partial r}\left(\frac{1}{r}\frac{\partial}{\partial r}(ru_r)\right)+\frac{\partial^2 u_r}{\partial z^2} \quad (10)$$

Z-momentum
$$\epsilon^4 Re\left[\left(u_r\frac{\partial u_z}{\partial r}\right)+\left(u_z\frac{\partial u_z}{\partial z}\right)\right]=-\frac{\partial p}{\partial z}+\epsilon^2\left[\epsilon^2\left(\frac{1}{r}\frac{\partial}{\partial r}\left(r\frac{\partial u_z}{\partial r}\right)\right)+\left(\frac{\partial^2 u_z}{\partial z^2}\right)\right] \quad (11)$$

Energy Balance Equation
$$\epsilon^2 Pe\left[\left(u_r\frac{\partial \theta}{\partial r}\right)+\left(u_z\frac{\partial \theta}{\partial z}\right)\right]=\left[\epsilon^2\left(\frac{1}{r}\frac{\partial}{\partial r}\left(r\frac{\partial \theta}{\partial r}\right)\right)+\left(\frac{\partial^2 \theta}{\partial z^2}\right)\right] \quad (12)$$

Continuity Equation
$$\frac{1}{r}\frac{\partial}{\partial r}(ru_r)+\frac{\partial u_z}{\partial z}=0, \qquad U_z=\epsilon U_R \quad (13)$$

Interfacial and Bourndary Conditions		
Normal Stress Balance	$p = -\frac{1}{\delta}\left(\frac{\partial^2 h}{\partial r^2}\right)$	(14)
Tangential Stress Balance	$\frac{\partial u_r}{\partial z} + O(\epsilon^2) = \frac{\epsilon(\partial\gamma^*/\partial T^*)\Delta T}{\mu U_R}\left[\frac{\partial\theta}{\partial r} + \frac{\partial\theta}{\partial z}\frac{\partial h}{\partial r}\right]$	(15)
Heat Flux	$\left(-\epsilon^2\frac{\partial h}{\partial r}\right)\frac{\partial\theta}{\partial r} + \frac{\partial\theta}{\partial z} = q$	(16)

In Table 4, $h(r)$ is the non-dimensional geometry of the surface, $\epsilon = \frac{z_c}{l_c}$, is the ratio of characteristic length scales in the z and r directions, $Re = U_R l_c/\nu$ is the Reynolds number, $Pe = U_R l_c/\alpha$ is the Peclet number, $\delta = Ca/\epsilon^3$ is a non-dimensional parameter resulting from Capillary number $Ca = \mu U_R/\gamma_0$.

5 Thin film approximation

A thin film is defined as the region in which the characteristic depth scale is comparatively very smaller than the characteristic length scale. In case of pLSM, this translates to $\epsilon = \frac{z_c}{l_c} \ll 1$. An illustrative schematic of metpool in pLSM is shown in Figure 3. The resultant melt pool diameters are of the order of 30-50 μm and the resultant maximum melt pool are of the order of 3-5 μm [3,11], meaning that $\epsilon \sim O(-1)$. Therefore, approximation of the meltpool obtained in pLSM as a thin film is reasonable. The solution obtained thereof gives the general idea about velocity, and temperature distribution. A outcome of particular interest in this paper is the semi-analytical solution for evolved interfacial height function.

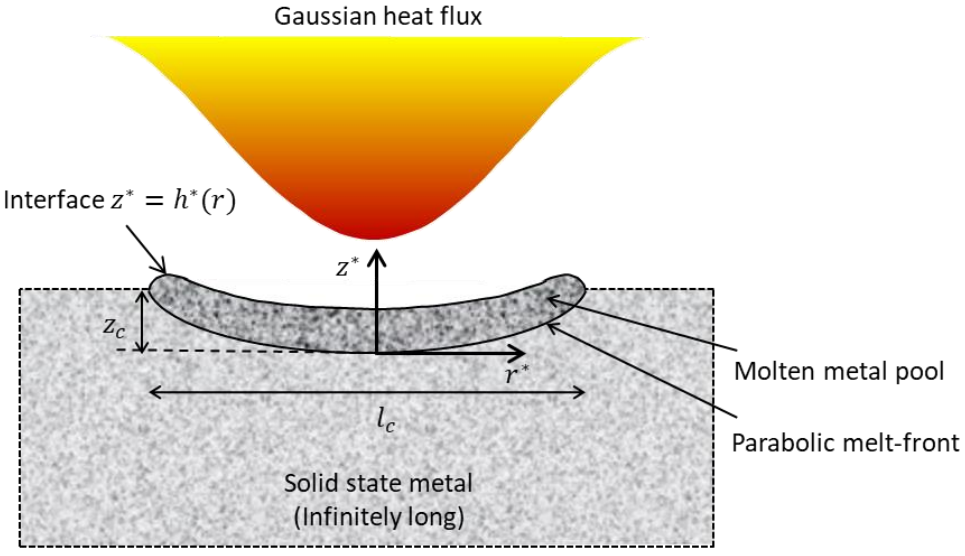

Figure 3: Thin Film domain of dimension $\boldsymbol{z_c}$ x $\boldsymbol{l_c}$

In additional to small ϵ, the following are assumptions are made for analysis. It is to be noted that some of these assumptions are invalid for all process conditions and the effects of the same will be discussed in later sections.

- Rescaled Reynolds number, defined as $\widehat{Re} = \epsilon Re$ and rescaled Peclet number, $\widehat{Pe} = \epsilon Pe$ are assumed to be $O(1)$.
- All dependent properties such as p, θ, u_r, u_z, and h can be expressed in asymptotic expansion in the thin film limit of $\epsilon \ll 1$. This can be mathematically expressed as:

$$\begin{aligned} p &= p^{(0)} + \epsilon p^{(1)} + \epsilon^2 p^{(2)} + ... \\ \theta &= \theta^{(0)} + \epsilon \theta^{(1)} + \epsilon^2 \theta^{(2)} + ... \\ u &= u^{(0)} + \epsilon u^{(1)} + \epsilon^2 u^{(2)} + ... \\ h &= h^{(0)} + \epsilon h^{(1)} + \epsilon^2 h^{(2)} + ... \end{aligned} \tag{17}$$

Under these assumptions and neglecting all terms of the order ϵ^2 or higher in Equations (10) - (17), the simplified process equations can be rewritten as follows. More details are available in Appendix B.

$$\frac{1}{r}\frac{\partial}{\partial r}\left(r u_r^{(0)}\right) + \frac{\partial u_z^{(0)}}{\partial z} = 0, \tag{18}$$

$$\frac{\partial^2 \theta^{(0)}}{\partial z^2} = 0 \tag{19}$$

$$\frac{\partial^2 u_r^{(0)}}{\partial z^2} - \frac{\partial p^{(0)}}{\partial r} = 0 \tag{20}$$

$$\frac{\partial p^{(0)}}{\partial z} = 0 \tag{21}$$

$$p^{(0)} = -\frac{1}{\delta}\left(\frac{\partial^2 h}{\partial r^2}\right) \tag{22}$$

$$\frac{\partial u_r^{(0)}}{\partial z} = \frac{\partial \theta^{(0)}}{\partial r} + \frac{\partial \theta^{(0)}}{\partial z}\frac{\partial h}{\partial r} \tag{23}$$

$$\frac{\partial \theta^{(0)}}{\partial z} = q \tag{24}$$

5.1 Lower boundary of thin film

Usually, thin film analysis assumes a rectangular shape of the film, where both the top and the bottom boundaries are flat. In case of pLSM, the meltfront, which is boundary of the meltpool is rarely flat. This is especially true when the melt pool sizes are large. Therefore, in this paper, both flat as well as curved meltpool boundairs are considered. Further, based on numerical and experimental observations [11,22], the curved meltpool boundary is approximated as a parabolic curve. A typical melt front created observed in simulations is shown in Figure 4, along with a parabolic curve with suitable coefficients. The dimensional and non-dimensional

parabolic boundary, along with the corresponding boundary conditions are mathematically given by,

$$T^* = T_l \;\&\; \underline{V}^* = 0, \qquad @h^* = f^*(r^*) = \begin{cases} 0, & flat\ meltfront \\ Kr^{*2} + \beta, & parabolic\ meltfront \end{cases} \tag{25}$$

$$\theta = 0 \;\&\; u_{r,z} = 0, \qquad @h = f(r) = \begin{cases} 0, & flat\ meltfront \\ \hat{K}r^2 + \hat{\beta}, & parabolic\ meltfront \end{cases} \tag{26}$$

where K and β are constants. $\hat{K} = Kl_c^2/z_c$, $\hat{\beta} = \beta/z_c$ are the coefficient that are functions of characteristic length scales.

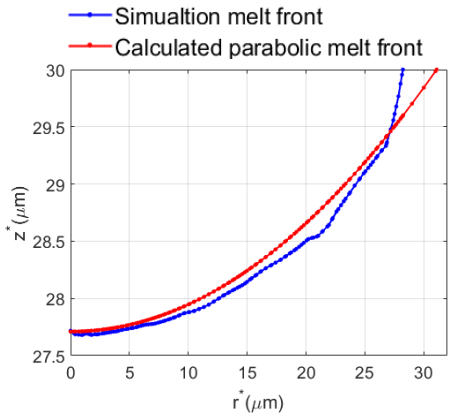

Figure 4: Melt front shape with a parabolic fit

5.2 Solution of surface height

In this section, a steady state solution to the surface height, $h(r)$, is derived under the thin film approximation of the melt pool created in pLSM. For conciseness, only the key details are provided in the section, while the detailed derivation is provided in Appendix B.

To begin with the solution, Equation (19) for leading-order temperature, $\theta^{(0)}$ is solved under heat flux boundary condition in Equation (24) and constant temperature boundary condition in Equation (26),

$$\theta^{(0)} = q(r)\big(z - f(r)\big) \tag{27}$$

where $f(r)$ is the meltfront geometry as defined in Equation (26) and $q(r) = C\, e^{-8r^2}$. The constant C is defined in Appendix A.

The solution for leading-order velocity, $u_r^{(0)}$ can be found from Equations (20) and (23) under the boundary condition in Equation (26) and is given by,

$$u_r^{(0)} = \frac{\partial p^{(0)}}{\partial r}\frac{z^2}{2} + \left(A - \frac{\partial p^{(0)}}{\partial r}h\right)z - \frac{\partial p^{(0)}}{\partial r}\frac{f(r)^2}{2} - \left(A - \frac{\partial p^{(0)}}{\partial r}h\right)f(r) \tag{28}$$

where, $A = q'(r)\big(h - f(r)\big) + q(r)\big(-f'(r)\big) + \frac{dh}{dr}\, q(r)$

Given that there is no loss of material in the melt pool, a zero net volume flux condition can be imposed as follows,

$$\int_0^{h(r)} u_r^{(0)}(r,z)dz = 0 \tag{29}$$

Substituting from (28), Equation (29) gives the pressure gradient as,

$$\frac{\partial p^{(0)}}{\partial r} = \frac{A\left(f(r) - \frac{h}{2}\right)}{\left(-\frac{h^2}{3} - \frac{f(r)^2}{2} + hf(r)\right)} \tag{30}$$

Finally, differentiating normal stress balance condition in Equation (22) with respect to r, $\partial p^{(0)}/\partial r$ from Equation (30) can be eliminated, resulting in,

$$\frac{d^3h}{dr^3} = \frac{\delta\left[\, q'(r)\big(h - f(r)\big) + q(r)(-f'(r)) + \frac{dh}{dr}\, q(r)\right]\left(f(r) - \frac{h}{2}\right)}{\left(-\frac{h^2}{3} - \frac{f(r)^2}{2} + hf(r)\right)} \tag{31}$$

A closed form solution to Equation (31) cannot be obtained. However, in the limit of $\epsilon \ll 1$, the deformation is small enough. Therefore, the $O(\epsilon^2)$ and higher order terms can be neglected in the expression of h in Equation (17) to obtain an approximate solution in the form of

$$h(r) = h^{(0)}(r) + \epsilon h^{(1)}(r) \tag{32}$$

Equations (31) and (32), yield two expression for the leading-order term, $h^{(0)}$ and the first-order term, $h^{(1)}$. The detailed derivation of these expressions is in documented in Appendix B. At $O(1)$, a trivial solution of $h^{(0)}$ emerges as,

$$h_0(r) = 1 \tag{33}$$

And the first-order term, $h^{(1)}$ becomes,

$$\frac{d^3h^{(1)}}{dr^3} = 6\delta C e^{-8r^2}\big[16r\big(1 - f(r)\big) + f'(r)\big]\, \frac{(f(r) - 0.5)}{(3f(r)^2 - 6f(r) + 2)} \tag{34}$$

While there is no analytical solution for $h^{(1)}$, Equation (34) can be numerically integrated for the two boundary functions $f(r)$. Substituting both in Equation (32), thus results in a solution to the surface height of the meltpool in pLSM.

Solution for $h_1(r)$, combined with $h_0(r)$ gives a semi-analytical solution for interfacial height function $h(r)$ as,

$$h(r) = h_0(r) + \epsilon h_1(r) \tag{35}$$

5.3 Method of validation

In order to validate the thin-film approximate solution for the steady state surface height of the meltpool, comparison are made with the detailed numerical model described earlier. Note that the numerical model itself was validated against experimental results from literature [11].

These are summarized in Table 2. Comparisons for validation will be made at nine different pulse duration on an initially flat surface. The pulse energy for each pulse duration is chosen such that maximum temperature in the numerical simulation is just below the ablation temperature. This is hypothesized to provide sufficient time for the meltpool flows to reach steady state. It will be shown in later discussion that this has limitations.

To have a meaningful comparision of the solution from thin film approximation with the numerical solution, non-dimensionalizing characteristic values, z_c and l_c are required. These characteristic values have to be chosen diffrerently for the two solution methods to properly non-dimesionalize the results. For numerical results, z_c is chosen as maximum melt depth defined as maximum penetration of the melt front from initial flat surface and l_c is chosen the farthest radial reach of the meltfront. The values for each pulse duration are tabulated in Table 5.

For thin film approximation, z_c is chosen based on theoretical analysis done in [13], wherein the authors present given an analytical solution of maximum underestimated value, $h_{11\,max}$ and overestimated value, $h_{12\,max}$ for pulsed laser induced melt depth, based on simple heat conduction model valid for any material/alloy. In the current work, z_c is chosen as an average of $h_{11\,max}$ and $h_{12\,max}$. It can be seen from Table 5, that the analytical approximation of Tokarev et al. [13] and the numerical solution sufficiently close. There are no suitable analytical approximations for the characteristic length, l_c. Therefore, the full-width-half-maximum of the assumed gaussian beam is chosen as a constant l_c for all pulse durations. In reality, this is a poor choice as the melt pool size inceases with increasing pulse duration. However, addressing this is beyond the scope of the current work.

Table 5: Characteristic length values used for non-dimensionalize the results at different pulse durations

$t_p(\mu s)$	Pulse Energy (mJ)	Length scales used to nondimensionalize numerical solution		Length scales used to nondimensionalize thin film approximation results	
		$z_c(\mu m)$	$l_c(\mu m)$	$z_c(\mu m)$	$l_c(\mu m)$
0.5	265	2.30	62.10	2.29	62.18
0.8	336	2.88	65.46	2.90	62.18
1.0	380	3.05	67.96	3.24	62.18
1.2	408	3.46	67.49	3.55	62.18
1.5	473	3.94	66.80	3.97	62.18
2.0	564	4.72	70.63	4.58	62.18
3.0	720	5.87	74.43	5.61	62.18
4.0	860	6.95	77.51	6.48	62.18
5.0	975	7.80	77.24	7.24	62.18

6 Results and discussion

Figure 5 shows nine different cases with final interfacial surface profile of simulation height (black color) and thin film approximation height for flat melt fron (red color) and parabolic melt-front (blue color) under various pulse duration values. Figure 5 also shows the percentage error plots for thin film predictions with respect to the numerical results. The error is quantified using two metrics namel, Mean Absolute Percentage Error (MAPE) and Root Mean Square Error (RMSE), for the two melt-front geometries. In general, the solution with parabolic melt front matches closely with the solution with a flat melt front. However, there are few caveats and are discussed in the following.

Observation 1

Figure 5 (a), (b) and (c) compare the thin film surface geometry estimation to surface evolution from the numerical solution for smaller pulse durations ($t_p = 0.5, 0.8$ and $1.0\ \mu s$). The RMSE errors are 11%, 7% and 5% respectively with a flat meltfront geometry and 15%, 10% and 8% for a parabolic meltfront.

It can be seen that the solution obtained by thin film overestimates the surface height as compared to the numerical results. This is because thin film is a steady state solution while numerical model accounts for transients of the flows. Further, the thin film does not account for phase change. It assumes that the melt pool is always in liquidus state. On the other hand, phase change is accounted for in the numerical solutions. At smaller pulse durations, it is possible that the melt pool resolidifies before reaching a steady state. In other words, the flows do not have sufficient time to reach a steady state. Therefore, the steady state thin film solution over-estimates the surface geometry as compared to the transient numerical solution. To support the above discussed argument, further analysis and investigation is required which is beyond the scope of the current work. Nonethless, the errors in these three cases range from 5% to 15% RMSE value across the two geometries and quite useful in predicting the overall surface features and roughness of the surface.

Observation 2

For longer pulse durations, $t_p = 3, 4$ and $5\ \mu s$, shown in Figure 5 (g), (h) and (i), The RMSE errors are ~17%, ~24% and ~26% respectively with a flat meltfront geometry and ~15%, ~23% and ~25% for a parabolic meltfront.

Here, the thin film solution underestimates the numerical solution. At these longer pulse durations, dominance of thermocapillary flows result in more upwelling of surface from center towards outwards. In thin film approximation study, only the $O(1)$ solution was considered, neglecting higher order terms. Further, the rescaled Peclect number, $\widehat{Pe}$ and the rescaled Reynolds number, $\widehat{Re}$ are assumed to be of $O(1)$. The values of $\widehat{Pe}$ and $\widehat{Re}$ are tabulated in Table 6. While the values of $\widehat{Pe}$ are of $O(1)$, $\widehat{Re}$ values are of $O(2)$. At higher pulse durations, deeper melt pools coupled with dominating thermocapillary flows result in significantly higher velocities of flows. However, the velocity scale assumed for thin film does not capture this effect and therefore violates the assumption of $\widehat{Re} \sim O(1)$. Further, Table 6 also shows the value of parameter ϵ increases with pulse duration. It is also assumed that $\epsilon \ll 1$ ensures the thin film approximation validity. Therefore, the high value of ϵ indicates that, at the high pulse duration

values, thin film cannot approximate the surface height, and therefore significant underestimation is observed.

Observation 3

For intermediate pulse durations, $t_p = 1.2, 1.5$ and $2\ \mu s$ values i.e., from Figure 5 (c), (d), (e), thin film approximation results closely estimate of final evolved surface height as predicted by numerical results. The RMSE errors are ~5%, ~4% and ~8% respectively with a flat meltfront geometry and ~6%, ~5% and ~7% for a parabolic meltfront. This demonstrates the immediate applicability of thin film solution at these intermediate pulse durations.

Figure 6 shows the trend of both errors MAPE and RMSE for flat and parabolic melt front with respect to t_p. Figure confirms that MAPE and RMSE in the range of pulse duration of 1.2 to 2 μs are minimum. The maximum RMSE of 26.43% is captured at $5\ \mu s$ pulse duration and minimum MAPE 3.53% is captured at $1.2\ \mu s$ pulse duration for flat shape thin film from Figure 5. It can be seen from the Figure 6 (a) and (b) that the solution with flat melt front approximation has a smaller error as compared to the parabolic melt front approximation. This is quite intuitive as at small pulse durations, the pools are very shallow, and the melt front is much closer to being flat than parabolic. Figure 6 (c) and (d) are also in agreement with lowest errors at intermediate pulse durations $1.2, 1.5$ and $2\ \mu s$.

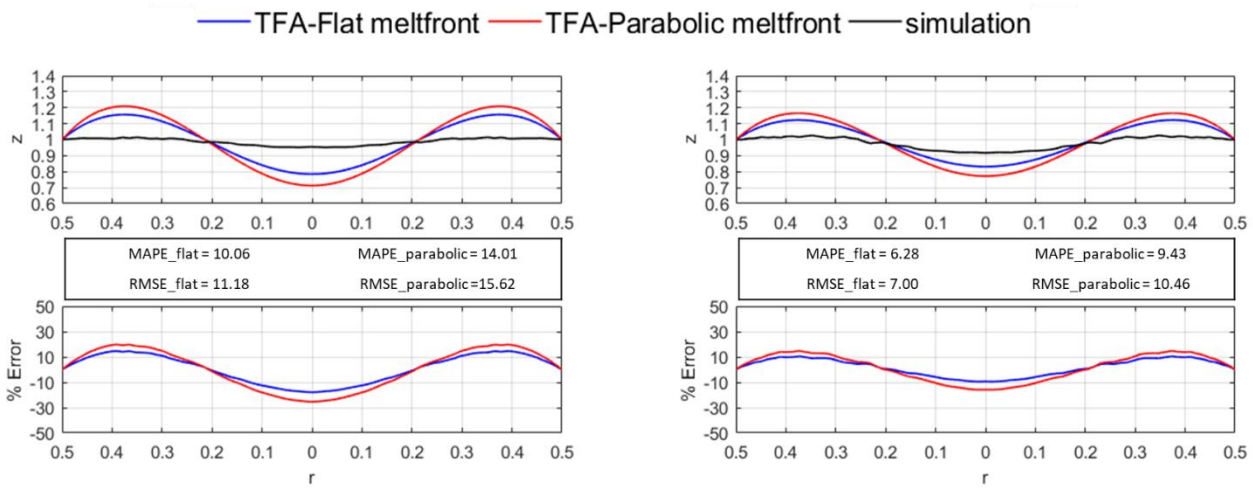

(a) $t_p = 0.5\ \mu s$ (b) $t_p = 0.8\ \mu s$

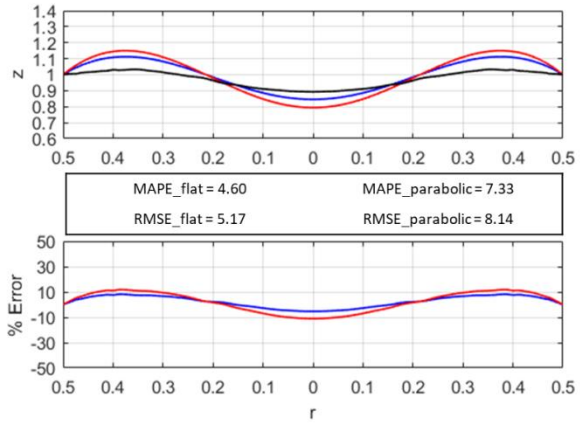

(c) $t_p = 1\ \mu s$

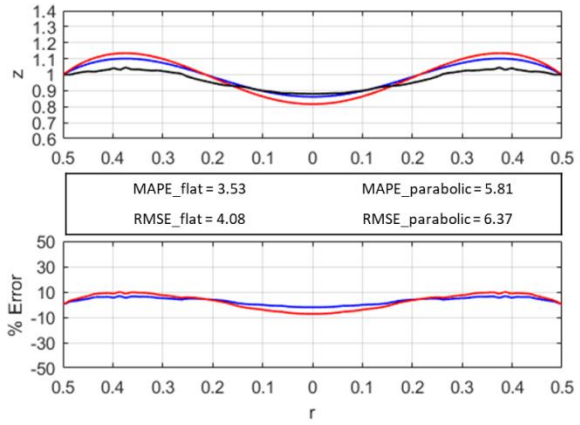

(d) $t_p = 1.2\ \mu s$

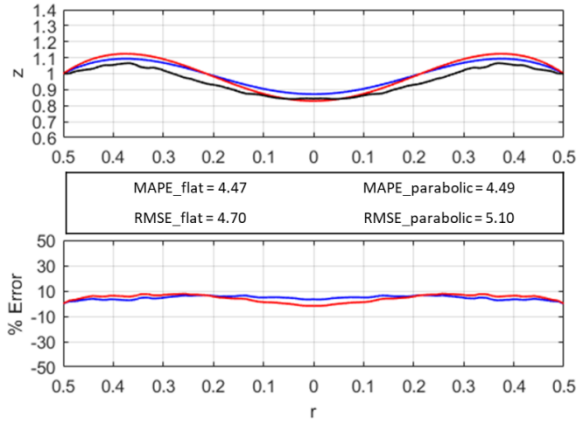

(e) $t_p = 1.5\ \mu s$

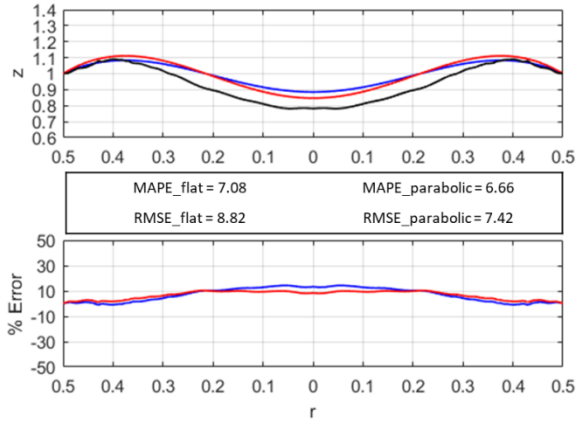

(f) $t_p = 2\ \mu s$

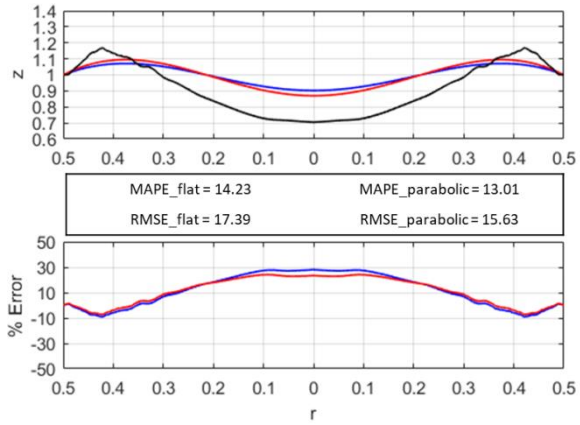

(g) $t_p = 3\ \mu s$

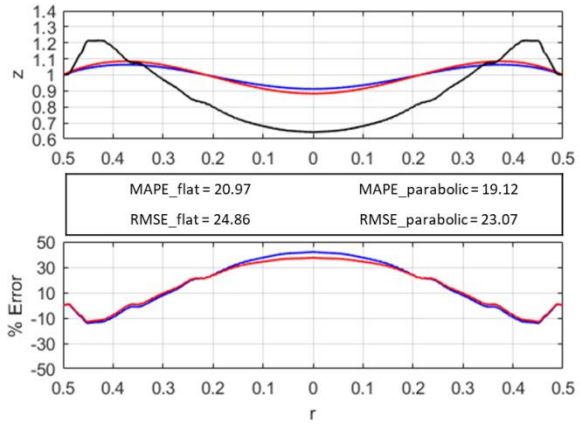

(h) $t_p = 4\ \mu s$

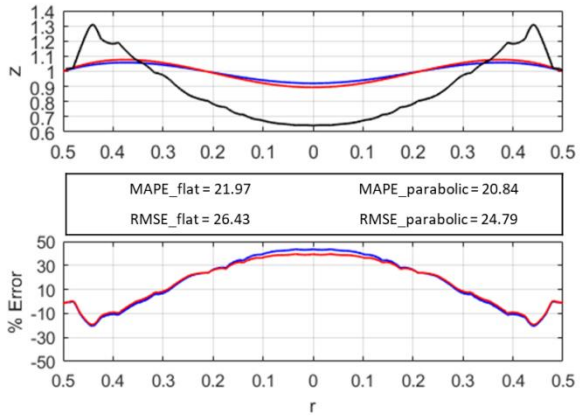

(i) $t_p = 5\ \mu s$

Figure 5: Comparisons for simulation and semi-analytical solution at different pulse durations

Table 6: Parameter $\boldsymbol{\epsilon}$, Peclet, Reynolds number from TFA analysis

$\boldsymbol{t_p(\mu s)}$	$\boldsymbol{\epsilon = z_c/l_c}$	$\widehat{\boldsymbol{Pe}}$	$\widehat{\boldsymbol{Re}}$
0.5	0.037	0.716	5.37
0.8	0.046	1.150	8.62
1	0.052	1.434	10.76
1.2	0.057	1.722	12.92
1.5	0.064	2.153	16.15
2	0.074	2.866	21.50
3	0.090	4.301	32.26
4	0.104	5.738	43.04
5	0.116	7.163	53.72

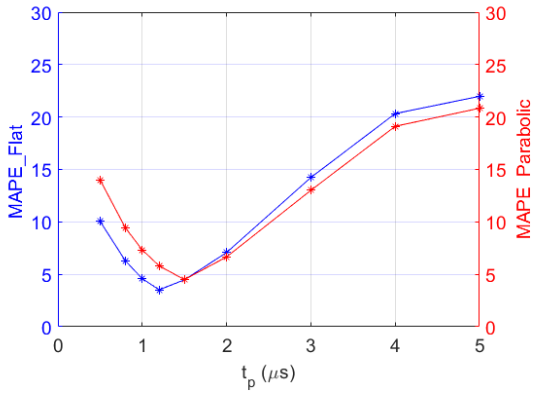

(a)

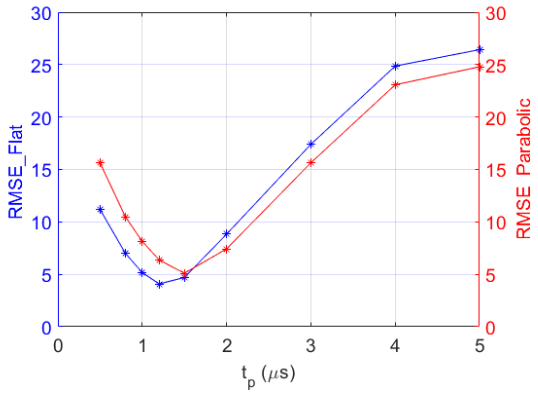

(b)

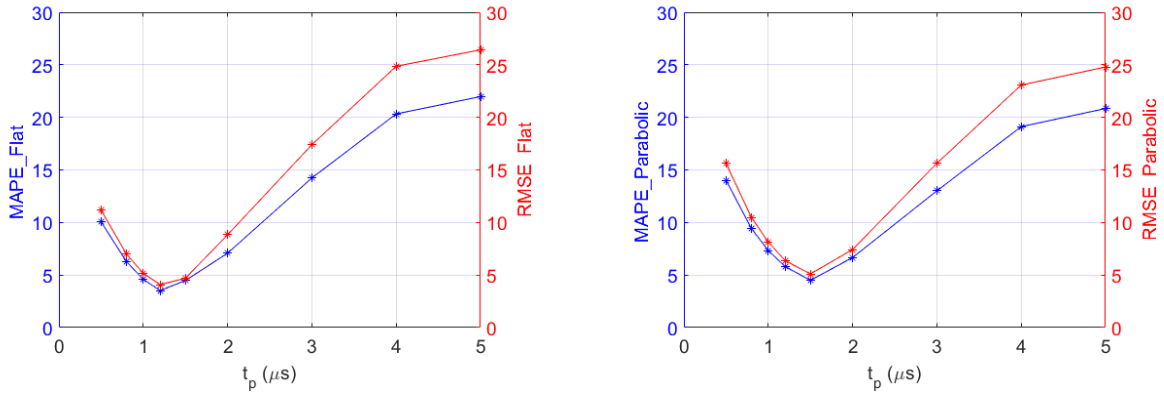

(c) (d)

Figure 6: MAPE and RMSE for parabolic melt-front profile with respect to pulse duration

7 Conclusion and future work

This paper presents a steady state semi-analytical solution to evaluate the evolved surface geometry under pulsed laser surface melting. The solution models the meltpool as a thin film motivated by the observation that typical ratio of meltpool diameters to melt depths, ϵ are very small. The thin film solution also assumes temperature independent material properties. Further, the thin film solution accounts for two geometries of the melt pool shapes, namely a flat lower boundary and a parabolic lower boundary. The paper also discusses a transient axisymmetric numerical solution for pulsed laser surface melting that accounts for temperature dependent properties to study the evolution of surface geometry. To validate the numerical model, the evolved surface heights were compared with results from literature and the results closely match each other. Finally, the thin film solution of evolved surface geometry was compared with that of the numerical model. The comparisons were carried for different pulse durations and pulse energies on initially flat surface surface under similar process conditions.

The final evolved surface height from both the models demonstrate a reasonable match with the root mean square errors ranging from ~4% to ~25%. Larger errors are observed at comparatively lower and higher pulse duration and smaller errors are observed for intermediate pulse duration values. It was observed that at lower pulse duration, the steady state assumption may be violated as the time required for the flows to reach a steady state may be larger than the time required for resolidification. At larger pulse durations the melt depths become larger, thus resulting in higher values of ϵ. Further, it was also observed that thin film solution with a flat boundary predicts better at lower pulse duration and that with a parabolic shape is more suitable for higher pulse durations.

Overall, the thin film solution is a a reasonable and useful approximation of the of the evolved surface geometry through pLSM process, thus saving significant computational costs. This paper clearly articulates the limitations of thin film approximations for pLSM and thus motivates for further modelling improvements and considerations of higher orders of ϵ.

Acknowledgment

The authors thank Prof. Uddipta Ghosh, Assistant Professor, IIT Gandhinagar for his valuable inputs and IIT Gandhinagar for supporting this work.

Funding

This work was supported by the Indian Institute of Technology Gandhinagar, Gandhinagar, Gujarat, India.

References

[1] Bordatchev EV, Hafiz AMK, Tutunea-Fatan OR. Performance of laser polishing in finishing of metallic surfaces. Int J Adv Manuf Technol 2014;73:35–52. https://doi.org/10.1007/s00170-014-5761-3.

[2] Perry T, Werschmoeller D, Li X, Pfefferkorn F, Duffie N. Micromelting for Laser Micro Polishing of Meso/Micro Metallic Components, 2007. https://doi.org/10.1115/MSEC2007-31173.

[3] Vadali M, Ma C, Duffie NA, Li X, Pfefferkorn FE. Effects of Pulse Duration on Laser Micro Polishing. Journal of Micro and Nano-Manufacturing 2013;1:011006. https://doi.org/10.1115/1.4023756.

[4] Chow MTC, Bordatchev EV, Knopf GK. Experimental study on the effect of varying focal offset distance on laser micropolished surfaces. The International Journal of Advanced Manufacturing Technology 2013;67:2607–17. https://doi.org/10.1007/s00170-012-4677-z.

[5] Nüsser C, Wehrmann I, Willenborg E. Influence of Intensity Distribution and Pulse Duration on Laser Micro Polishing. Physics Procedia 2011;12:462–71. https://doi.org/10.1016/j.phpro.2011.03.057.

[6] Miller JD, Tutunea-Fatan OR, Bordatchev EV. Experimental Analysis of Laser and Scanner Control Parameters During Laser Polishing of H13 Steel. Procedia Manufacturing 2017;10:720–9. https://doi.org/10.1016/j.promfg.2017.07.029.

[7] Basu B, Srinivasan J. Numerical study of steady-state laser melting problem. International Journal of Heat and Mass Transfer 1988;31:2331–8. https://doi.org/10.1016/0017-9310(88)90164-0.

[8] Qu Y, Choi H, Perry T, Jeon Y, Pfefferkorn F, Li X, et al. Numerical and Experimental Investigation of Micromelting for Laser Micro Polishing of Meso/Micro Metallic Components 2006:1063–70. https://doi.org/10.1115/MSEC2006-21126.

[9] Zhang C, Zhou J, Shen H. Role of Capillary and Thermocapillary Forces in Laser Polishing of Metals. J Manuf Sci Eng 2017;139:041019-041019–11. https://doi.org/10.1115/1.4035468.

[10] Srinivasan J, Basu B. A numerical study of thermocapillary flow in a rectangular cavity during laser melting. International Journal of Heat and Mass Transfer 1986;29:563–72. https://doi.org/10.1016/0017-9310(86)90090-6.

[11] Ma C, Vadali M, Duffie NA, Pfefferkorn FE, Li X. Melt Pool Flow and Surface Evolution During Pulsed Laser Micro Polishing of Ti6Al4V. Journal of Manufacturing Science and Engineering 2013;135:061023. https://doi.org/10.1115/1.4025819.

[12] Woodard PR, Dryden J. Thermal analysis of a laser pulse for discrete spot surface transformation hardening. Journal of Applied Physics 1999;85:2488. https://doi.org/10.1063/1.369610.
[13] Tokarev VN, Kaplan AFH. An analytical modeling of time dependent pulsed laser melting. Journal of Applied Physics 1999;86:2836–46. https://doi.org/10.1063/1.371132.
[14] Sim B-C, Kim W-S. Melting and dynamic-surface deformation in laser surface heating. International Journal of Heat and Mass Transfer 2005;48:1137–44. https://doi.org/10.1016/j.ijheatmasstransfer.2004.08.032.
[15] Zheng L, Zhang X, Gao Y. Analytical solution for Marangoni convection over a liquid–vapor surface due to an imposed temperature gradient. Mathematical and Computer Modelling 2008;48:1787–95. https://doi.org/10.1016/j.mcm.2008.04.003.
[16] Kou S, Sun DK. Fluid flow and weld penetration in stationary arc welds. MTA 1985;16:203–13. https://doi.org/10.1007/BF02815302.
[17] Mills KC. Recommended values of thermophysical properties for selected commercial alloys 2002. Cambridge: Woodhead.
[18] Rai R, Burgardt P, Milewski JO, Lienert TJ, DebRoy T. Heat transfer and fluid flow during electron beam welding of 21Cr–6Ni–9Mn steel and Ti–6Al–4V alloy. Journal of Physics D: Applied Physics 2008;42:025503. https://doi.org/10.1088/0022-3727/42/2/025503.
[19] Brandes EA, Brook GB. Smithells Metals Reference Book. Elsevier; 2013.
[20] Boyer Rodney, Welsch Gerhard, Collings EW. Materials properties handbook : titanium alloys 1994. Materials Park, OH: ASM International.
[21] Solutions to Linear Systems of Equations: Direct and Iterative Solvers | COMSOL Blog n.d. https://www.comsol.com/blogs/solutions-linear-systems-equations-direct-iterative-solvers/ (accessed May 29, 2020).
[22] Vadali VM. Advanced Study of Pulsed Laser Micro Polishing. University of Wisconsin - Madison, 2013.
[23] Leal LG. Advanced Transport Phenomena: Fluid Mechanics and Convective Transport Processes. Cambridge: Cambridge University Press; 2007. https://doi.org/10.1017/CBO9780511800245.

Appendix A. Derivation of Non-dimensional Process Model

To non-dimesionalize the process model, length, velocity and temperature are scaled with appropriate characteristic values as follows:

$$u_r = \frac{u_r^*}{U_R}, u_z = \frac{u_z^*}{U_z}, \qquad r = \frac{r^*}{l_c}, z = \frac{z^*}{z_c}, \epsilon = \frac{z_c}{l_c}$$
$$\theta = \frac{T^* - T_l}{\Delta T} \tag{A. 1}$$

where, θ is nondimensional temperature, T_l is liquidus temperature, $\Delta T = (T_v - T_l)$ is difference between ablation, T_v and liquidus temperature, T_l. The choice of length scales is discussed in Section 5.3 and the velocity scales will emerge from the non-dimetionalization in the following.

Continuity equation

Using the scaling in Equation (A. 1), the non-dimesional continuity equation can be written as follows:

$$\frac{1}{r}\frac{\partial}{\partial r}(ru_r) + \frac{\partial u_z}{\partial z} = 0, \qquad U_z = \epsilon U_R \tag{A. 2}$$

It can be seen that the reatio velocity scales is same as the ratio of length scales, ϵ. This is rather intuitive given the assumption of steady state.

Energy equation

Upon steady state condition of temperature and the scaling in Equation (A. 1) on the dimestional energy equation in Equation (1), the non-dimensional energy equation is derived as,

$$\epsilon^2 Pe\left[\left(u_r\frac{\partial\theta}{\partial r}\right) + \left(u_z\frac{\partial\theta}{\partial z}\right)\right] = \left[\epsilon^2\left(\frac{1}{r}\frac{\partial}{\partial r}\left(r\frac{\partial\theta}{\partial r}\right)\right) + \left(\frac{\partial^2\theta}{\partial z^2}\right)\right] \tag{A. 3}$$

where, $\boldsymbol{Pe}$ is the Peclet number, defined as $\boldsymbol{U_R l_c/\alpha}$.

Fluid flow equation

For simplicity, Navier-Stokes equation in Equation (2) can be separated into the $\boldsymbol{R}$-momentum and $\boldsymbol{Z}$-momentum equations, with the steady state assumption imposed as,

R-momentum
$$u_r^*\frac{\partial u_r^*}{\partial r^*} + u_z^*\frac{\partial u_r^*}{\partial z^*} = -\frac{1}{\rho}\frac{\partial p^*}{\partial r^*} + \nu\left[\frac{\partial}{\partial r^*}\left(\frac{1}{r^*}\frac{\partial}{\partial r^*}(r^* u_r^*)\right) + \frac{\partial^2 u_r^*}{\partial z^{*2}}\right] \tag{A. 4}$$

Z-momentum
$$u_r^*\frac{\partial u_z^*}{\partial r^*} + u_z^*\frac{\partial u_z^*}{\partial z^*} = -\frac{1}{\rho}\frac{\partial p^*}{\partial z^*} + \nu\left[\left(\frac{1}{r^*}\frac{\partial}{\partial r^*}\left(r^*\frac{\partial u_z^*}{\partial r^*}\right)\right) + \frac{\partial^2 u_z^*}{\partial z^{*2}}\right]$$

Using the scaling given in Equation (A. 1), these are simplified to,

R-momentum $$\epsilon^2 Re\left[\left(u_r\frac{\partial u_r}{\partial r}\right)+\left(u_z\frac{\partial u_r}{\partial z}\right)\right]=-\frac{\partial p}{\partial r}+\epsilon^2\frac{\partial}{\partial r}\left(\frac{1}{r}\frac{\partial}{\partial r}(ru_r)\right)+\frac{\partial^2 u_r}{\partial z^2} \quad \text{(A. 5)}$$

Z-momentum $$\epsilon^4 Re\left[\left(u_r\frac{\partial u_z}{\partial r}\right)+\left(u_z\frac{\partial u_z}{\partial z}\right)\right]=-\frac{\partial p}{\partial z}+\epsilon^2\left[\epsilon^2\left(\frac{1}{r}\frac{\partial}{\partial r}\left(r\frac{\partial u_z}{\partial r}\right)\right)+\left(\frac{\partial^2 u_z}{\partial z^2}\right)\right]$$

where $\boldsymbol{Re}$ is Reynolds number defined as $\boldsymbol{U_R l_c/\nu}$. Note that in non-dimesionalizing the $\boldsymbol{R}$-momentum equation, a pressure scale emerges and is given by, $\boldsymbol{p_c=\frac{\mu U_R l_c}{z_c^2}}$.

Interfacial normal stress balance

Equation (4) balances normal stresses and consists of pressure, viscous stress tensor and curvature terms. The viscous stress tensor and normal to surface are given by,

$$\underline{\underline{\tau^*}}=\mu\left[\left(\underline{\nabla}^*\,\underline{V}^*\right)+\left(\underline{\nabla}^*\,\underline{V}^*\right)^T\right] \quad \text{(A. 6)}$$

$$\hat{n}=\frac{\underline{\nabla}^*\left(z^*-h^*(r)\right)}{|\underline{\nabla}^*\left(z^*-h^*(r)\right)|}=\widehat{e_z}-\epsilon\frac{\partial h}{\partial r}\widehat{e_r} \quad \text{(A. 7)}$$

where $h^*(r)$ is dimensional interfacial surface height as a function of the radial coordinate, which is subject of our interest as it decides the final evolution of interfacial surface. $h^*(r)$ is nondimensionalized by scale parameter z_c. Substituting Equations (A. 5) & (A. 6) in Equation (4) and scaling the dimensional quantities appropriately results in the non-dimensional normal stress balance equation as follows,

$$-p+O(\epsilon^2)\;=\frac{\epsilon^3\gamma^*}{\mu U_R}\left(\frac{\partial^2 h}{\partial r^2}\right) \quad \text{(A. 8)}$$

The surface tension γ^* can be assumed to vary linearly with temperature and is given by [23],

$$\begin{aligned}\gamma^* &= \gamma_0-(\partial\gamma^*/\partial T^*)(T^*-T_l)\\ &= \gamma_0\left[1-\frac{(\partial\gamma^*/\partial T^*)\theta\Delta T}{\gamma_0}\right]\end{aligned} \quad \text{(A. 9)}$$

As there is no significant effect of $(\partial\gamma^*/\partial T^*)\theta\Delta T/\gamma_0$ term in final solution [23], it can be neglected. Using capillary number defined as $Ca=\mu U_R/\sigma_0$ and parameter $\delta=Ca/\epsilon^3$, nondimensional Equation (A. 7) is rewritten as follows,

$$p=-\frac{1}{\delta}\left(\frac{\partial^2 h}{\partial r^2}\right) \quad \text{(A. 10)}$$

Interfacial tangential stress balance

On the same lines of normal stress balance, the tangential stress balance in Equation (5) can be normalized, wherein, the unit vector in the tangential direction at of the curved surface is given by

$$\hat{t}=\widehat{e_r}+\epsilon\frac{\partial h}{\partial r}\widehat{e_z} \quad \text{(A. 11)}$$

where, $<\widehat{e_r}, \widehat{e_z}>$ are the unit vectors in the r and z directions. Equation (5) is then non-dimesionalized using Equations (A. 1), (A. 6) and (A. 11), non-dimensional normal stress balance equations is given by,

$$\frac{\partial u_r}{\partial z} + O(\epsilon^2) = \frac{\epsilon(\partial\gamma^*/\partial T^*)\Delta T}{\mu U_R}\left[\frac{\partial\theta}{\partial r} + \frac{\partial\theta}{\partial z}\frac{\partial h}{\partial r}\right] \tag{A. 12}$$

Heat flux boundary condition

The incident laser beam is modelled as heat flux applied on top surface of material. This is given in Equation (6) and is non-dimensionalised as,

$$\left(-\epsilon^2\frac{\partial h}{\partial r}\right)\frac{\partial\theta}{\partial r} + \frac{\partial\theta}{\partial z} = q \tag{A. 13}$$

This also results in a characteristic flux scale, $q_c = k\Delta T/z_c$ that is used to non-dimensionalize the incident Gaussian flux in Equation (7). The resulting non-dimension flux, q, is given by,

$$q = \left[\frac{4\alpha P z_c}{k\Delta T\,\pi R_b^2}\right] e^{\left(-\frac{2r^{*2}}{R_b^2}\right)} = Ce^{(-8r^2)} \tag{A. 14}$$

wherein $l_c = 2R_b$ is used as the chanracteristic value in the r-direction.

Appendix B. Thin film solution of surface height

The leading order temperature solution is arrived simply by integrating Equation (19). This solution is given in Equation (27). Similarly, Equation (20) can be integrated to get a general solution for the leading order velocity term, $u_r^{(0)}$ as,

$$u_r^{(0)} = \frac{\partial p^{(0)}}{\partial r}\frac{z^2}{2} + Fz + G \tag{B. 1}$$

The constant F and G can be solved for by imposing (i) no-slip boundary condition at melt-front and (ii) interfacial tangential stress balance condition. There are re-written as follows for ease fo reading,

$$@z = f(r);\ u_r^{(0)} = 0 \ \ \Rightarrow 0 = \frac{\partial p^{(0)}}{\partial r}\frac{f(r)^2}{2} + F\,f(r) + G \tag{B. 2}$$

$$@z = h(r);\ \frac{\partial u_r^{(0)}}{\partial z} = \left(\frac{\partial \theta^{(0)}}{\partial r} + \frac{\partial h}{\partial r}\,\frac{\partial \theta^{(0)}}{\partial z}\right) \tag{B. 3}$$

Thus, Equation (B. 1) results in Equation (28), wherein the pressure gradient is given by Equation (30) and is re-written here for convenience.

$$\frac{\partial p^{(0)}}{\partial r} = \frac{A\left(f(r) - \frac{h}{2}\right)}{\left(-\frac{h^2}{3} - \frac{f(r)^2}{2} + hf(r)\right)} \tag{B. 4}$$

Finally, after differentiating normal stress balance condition Equation (22) with respect to r-coordinate gives,

$$\frac{\partial p^{(0)}}{\partial r} = -\frac{1}{\delta}\left(\frac{d^3h}{dr^3}\right) \tag{B. 5}$$

Substituting for $\partial p^{(0)}/\partial r$ in Equation (30) results in a third order differential equation in surface height $h(r)$ (as shown in Equation (31)),

$$\frac{d^3h}{dr^3} = \frac{\delta\left[\,q'(r)\big(h - f(r)\big) + q(r)(-f'(r)) + \frac{dh}{dr}\,q(r)\right]\left(f(r) - \frac{h}{2}\right)}{\left(-\frac{h^2}{3} - \frac{f(r)^2}{2} + hf(r)\right)} \tag{B. 6}$$

Analytical solution to Equation (B. 6) cannot be obtained. However, in the limit of $\epsilon \ll 1$, the deformation is small enough to obtain an approximate solution in the form of,

$$h(r) = h^{(0)}(r) + \epsilon h^{(1)}(r) + \epsilon^2 h^{(2)}(r) + .. \tag{B. 7}$$

By substituting Equation (B. 6) in Equation (B. 7), we have,

$$\frac{d^3h^{(0)}}{dr^3} + \epsilon\left\{\frac{d^3h^{(1)}}{dr^3} - \frac{\delta\left[\,q'(r)\left(h^{(0)} - f(r)\right) + q(r)\left(-f'(r)\right) + \frac{dh^{(0)}}{dr}\,q(r)\right]\left(f(r) - \frac{h^{(0)}}{2}\right)}{\left(-\frac{{h^{(0)}}^2}{3} - \frac{f(r)^2}{2} + h^{(0)}f(r)\right)}\right\} + O(\epsilon^2) = 0 \tag{B. 8}$$

where, $h^{(0)}$ is given by, $\frac{d^3h^{(0)}}{dr^3} = 0$.

Assuming a generation solution of $h^{(0)}(r) = c_1r^2 + c_2r + c_3$ and imposing the boundary condition that the surface height does not change at the endges of the meltpool, i.e., $h^{(0)}(0.5) = h^{(0)}(-0.5) = 1$, results in a $c_1 = -c_2,\ \ c_3 = 1$.

Because there is no change in fluid mass or density, a constant-volume integral condition can be imposed within the melt pool as, i.e., $\int_{-0.5}^{0.5} h^{(0)}\,dr = 1$. This yields, $c_1 = c_2 = 0$. Therefor, the leading order trivial solution is given by,

$$h^{(0)}(r) = 1 \tag{B. 9}$$

Subsequently, the governing equation for $h^{(1)}(r)$ from Equation (B. 8) can be written as,

$$\frac{d^3h^{(1)}}{dr^3} = 6\delta C e^{-8r^2}\left[16r\left(1 - f(r)\right) + f'(r)\right]\frac{(f(r) - 0.5)}{(3f(r)^2 - 6f(r) + 2)} \tag{B. 10}$$

Although a close form solution for Equation (B. 10) does not exting, it can be numerically solved by mposing the same boundary conditions as those for $h^{(0)}(r)$, i.e. $h^{(1)}(-0.5) = h^{(1)}(0.5) = 1$ and $\int_{-0.5}^{0.5} h^{(1)}\,dr = 0$.

Finally, the leading order and the first order surface height values can be combined using in (B. 7) and ignoring higher order terms, the evolved surface geometry in pLSM can be predicted.